European Journal of Nuclear Medicine and Molecular Imaging (2021) 48:3075–3088
https://doi.org/10.1007/s00259-021-05251-0

ORIGINAL ARTICLE

Radiolabelling and preclinical characterization of ^{89}Zr-Df-radiolabelled bispecific anti-PD-L1/TGF-βRII fusion protein bintrafusp alfa

Ingrid Julienne Georgette Burvenich[1,2] · Yit Wooi Goh[1] · Nancy Guo[1] · Hui Kong Gan[1,2] · Angela Rigopoulos[1,2] · Diana Cao[1,2] · Zhanqi Liu[1,2] · Uwe Ackermann[2,3,4] · Christian Werner Wichmann[1,2] · Alexander Franklin McDonald[1,2] · Nhi Huynh[1] · Graeme Joseph O'Keefe[3,4] · Sylvia Jie Gong[3,5] · Fiona Elizabeth Scott[1,2] · Linghui Li[6] · Wanping Geng[6] · Anup Zutshi[6] · Yan Lan[6] · Andrew Mark Scott[1,2,3,4]

Received: 29 July 2020 / Accepted: 8 February 2021 / Published online: 19 February 2021

Abstract

Purpose This study aimed to optimize the ^{89}Zr-radiolabelling of bintrafusp alfa investigational drug product and controls, and perform the in vitro and in vivo characterization of ^{89}Zr-Df-bintrafusp alfa and ^{89}Zr-Df-control radioconjugates.

Methods Bintrafusp alfa (anti-PD-L1 human IgG1 antibody fused to TGF-β receptor II (TGF-βRII), avelumab (anti-PD-L1 human IgG1 control antibody), isotype control (mutated inactive anti-PD-L1 IgG1 control antibody), and trap control (mutated inactive anti-PD-L1 human IgG1 fused to active TGF-βRII) were chelated with *p*-isothiocyanatobenzyl-desferrioxamine (Df). After radiolabelling with zirconium-89 (^{89}Zr), radioconjugates were assessed for radiochemical purity, immunoreactivity, antigen binding affinity, and serum stability in vitro. In vivo biodistribution and imaging studies were performed with PET/CT to identify and quantitate ^{89}Zr-Df-bintrafusp alfa tumour uptake in a PD-L1/TGF-β-positive murine breast cancer model (EMT-6). Specificity of ^{89}Zr-Df-bintrafusp alfa was assessed via a combined biodistribution and imaging experiment in the presence of competing cold bintrafusp alfa (1 mg/kg).

Results Nanomolar affinities for PD-L1 were achieved with ^{89}Zr-Df-bintrafusp alfa and ^{89}Zr-avelumab. Biodistribution and imaging studies in PD-L1- and TGF-β-positive EMT-6 tumour-bearing BALB/c mice demonstrated the biologic similarity of ^{89}Zr-Df-bintrafusp alfa and ^{89}Zr-avelumab indicating the in vivo distribution pattern of bintrafusp alfa is driven by its PD-L1 binding arm. Competition study with 1 mg of unlabelled bintrafusp alfa or avelumab co-administered with trace dose of ^{89}Zr-labelled bintrafusp alfa demonstrated the impact of dose and specificity of PD-L1 targeting in vivo.

Conclusion Molecular imaging of ^{89}Zr-Df-bintrafusp alfa biodistribution was achievable and allows non-invasive quantitation of tumour uptake of ^{89}Zr-Df-bintrafusp alfa, suitable for use in bioimaging clinical trials in cancer patients.

Keywords PD-L1 · TGF-β · Bintrafusp alfa · Zirconium-89 · Immunotherapy

Ingrid Julienne Georgette Burvenich and Yit Wooi Goh contributed equally to this work.

This article is part of the Topical Collection on Oncology - General

✉ Andrew Mark Scott
andrew.scott@onjcri.org.au

[1] Tumour Targeting Laboratory, Olivia Newton-John Cancer Research Institute, 145 Studley Road, Heidelberg, Melbourne, Victoria 3084, Australia

[2] School of Cancer Medicine, La Trobe University, Melbourne, Australia

[3] Department of Molecular Imaging and Therapy, Austin Health, Melbourne, Australia

[4] Department of Medicine, University of Melbourne, Melbourne, Australia

[5] School of Engineering and Mathematical Sciences, La Trobe University, Melbourne, Australia

[6] EMD Serono Research & Development Institute, Inc., a business of Merck KGaA, Darmstadt, Germany, Billerica, MA, USA

Introduction

T cell–mediated anti-tumour response requires engagement of the T cell receptor on antigen-presenting cells as well as engagement of the B7 ligand family through the CD28 family of receptors. The B7 family comprises seven known members (B7.1, B7.2, ICOS-L, PD-L1, PD-L2, B4-H4, and B7-H3) [1]. Interaction of B7 family members with co-stimulatory receptors will increase the immune response. In contrast, interaction of B7 family members with co-inhibitory receptors will attenuate the immune response [2]. Tumour cells use the latter mechanism to suppress T cell–mediated killing. In recent years, new therapeutics targeting the co-inhibitory signalling pathways that lead to tumour immune suppression have seen impressive outcomes in clinical oncology [3–5]. Programmed death ligand 1 (PD-L1) has been identified as a key factor associated with poor clinical outcomes. Antibodies against PD-L1 and its receptor programmed death 1 (PD-1) have shown significant improvement in patient survival in different cancer groups (e.g. melanoma, lung cancer, renal cell cancer, head and neck cancer) [6–13]. Despite the improvements in clinical outcomes, only a subset of patients respond to PD-L1/PD-1 targeted therapies. In addition, some patients suffer severe toxicities (grade ≥ 3) in response to these therapies [6–10, 12]. Thus, there is a need to improve the objective response rate in patients as well as a need to develop diagnostic tools that can help with patient selection and prediction of toxicities.

Bintrafusp alfa (M7824) is an innovative first-in-class bifunctional fusion protein composed of the extracellular domain of the TGF-βRII receptor to function as a TGF-β "trap" fused to a human IgG1 antibody blocking PD-L1 [14]. Bintrafusp alfa simultaneously binds PD-L1 and TGF-β as demonstrated by two-step ELISA, thereby suppressing tumour growth and metastasis more effectively than treatment with either anti-PD-L1 or TGF-β trap alone [14–16]. Moreover, bintrafusp alfa is effective in combination with radiotherapy or chemotherapy [16]. This promising new strategy to target PD-L1 and TGF-β simultaneously has recently been supported by the works of Mariathasan et al. and Tauriello et al., demonstrating that dual inhibition of the TGF-β and PD-L1 pathways leads to tumour regression as a result of T cell penetration into so-called cold tumours [17, 18]. "Cold" tumours do not respond well to immunotherapy drugs because these tumours lack T cells. Increased TGF-β signalling has been found in the tumour microenvironment of non-responders to PD-1 and PD-L1 therapies thereby inhibiting the penetration of T cells in the tumour microenvironment and excluding T cells from the tumour microenvironment [17].

Clinical trials with bintrafusp alfa have commenced and early results indicate improved efficacy compared to current anti-PD-1/PD-L1 antibodies [19, 20]. Like PD-L1/PD-1 antibodies, the responses are durable, but not every patient responds to the same extent. SPECT and PET imaging of PD-L1 in mice has been reported demonstrating the feasibility of non-invasive in vivo imaging of PD-L1 expression in tumours utilizing radiolabelled antibody constructs [15, 21–26]. These studies have demonstrated efficient and specific uptake in PD-L1-expressing xenografts and monitored the impact of PD-L1-rich organs on the distribution of anti-PD-L1 antibodies. However, no prior study has explored the in vivo imaging properties of a novel construct targeting dual immune pathways including PD-L1. We report the development and characterization of ^{89}Zr-Df-bintrafusp alfa as a molecular imaging probe for PD-L1 and TGF-β expressed in tumours, thus providing evidence of the feasibility of this approach for extension into human trials.

Methods

Cell lines

Murine breast carcinoma cell line EMT-6 (ATCC CRL-2755 was obtained from the American Type Culture Collection (ATCC, Manassas, MD, USA). A human PD-L1 transfected HEK293 cell line (HEK293:hPDL1-17 cell line (HEK293/PD-L1)) was provided by EMD Serono Research Institute (Rockland, MA, USA). All cell lines tested negative for *Mycoplasma* and were cultured according to ATCC's recommended standard culture method.

Antibodies

Bintrafusp alfa (Batch 60112) and avelumab (Batch PD1G005) were obtained from Merck Serono S.p.A. (Italy). Isotype control (mutated inactive anti-PD-L1 control antibody) and trap control (mutated inactive anti-PD-L1 human IgG1 fused to active TGF-βRII) were obtained from EMD Serono Research Institute (USA).

Assessing binding activity of bintrafusp alfa and controls

Flow cytometry

PD-L1 binding was determined using HEK293/PD-L1 cells via flow cytometry. Briefly, 1×10^6 cells were incubated with 10 μg/mL of bintrafusp alfa or controls, followed by phycoerythrin conjugated goat anti-human IgG secondary $F(ab')_2$ antibody (Merck, P8047). Flow analysis was performed using FACS Canto II Flow Cytometry.

ELISA analysis

Binding to TGF-β isoforms (TGF-β1, TGF-β2, and TGF-β3) by bintrafusp alfa and controls was assessed by ELISA. Briefly, ELISA plates were coated with 0.5 μg/mL recombinant human TGF-β1, TGF-β2, or TGF-β3 (R&D Systems, Minneapolis, MN, USA) in phosphate-buffered saline incubated at room temperature overnight. Plates were blocked for non-specific binding with 1% bovine serum albumin in phosphate-buffered saline (pH 7.4) at room temperature for 1 h. Half-log serially diluted test samples from 10,000 to 0.0315 ng/mL were added to each well in duplicate. Following incubation at room temperature for 2 h, horse radish peroxidase conjugated goat anti-human IgG (Jackson Immunoresearch Laboratories, PA, USA) was used to detect bound antibody constructs and after extensive washings visualized with 3,3′,5,5′-tetramethylbenzidine (TMB) peroxidase substrate (Sigma-Aldrich, Castle Hill, NSW, Australia). The optical density (OD) was read at 450 nm using a SPECTROstar plate reader (BMG Labtech).

Antibody conjugation and radiolabelling

Bintrafusp alfa, avelumab, isotype control, and trap control were chelated with the bifunctional metal ion chelator *p*-isothiocyanatobenzyl-deferoxamine (Df-; Macrocyclics Inc., Dallas, TX, USA) at a 5.0-fold molar excess (DMSO concentration < 0.5%), similar to the method previously described by Vosjan et al. [27]. Details of the conjugation procedure are included in Online Resource Table 1. Prepared conjugates were purified via dialysis (Slide-A-Lyzer G2 10K MWCO, Thermo Fisher Scientific, USA) or Amicon Ultra Centrifugal filter (Ultracel 10K MWCO, Merck Millipore, Ireland) against 50 mM sodium acetate buffer (pH 5.6; BDH/VWR Chemicals, Australia) containing 5% w/v sorbitol and 0.01% w/v polysorbate 20, and stored at −80 °C. To assess retention of protein integrity following chelation, SDS-PAGE analysis was conducted on samples (2 μg) of each chelated antibody and compared to the native antibody constructs under both non-reduced and reduced conditions. NuPAGE™ gradient 4–12% Bis-Tris mini gels (Invitrogen) were run according to manufacturer's instructions. Suitable molecular weight markers were used to denote the elution position of the antibodies and protein bands were detected with Coomassie blue staining. Df-conjugates were analysed via LC-MS to determine the number of chelators per antibody. However, LC-MS spectra suffered from low SNRs and were inconclusive. Instead, chelator-to-antibody ratios were determined indirectly [28]. Briefly, aliquots of unpurified conjugation reaction mixtures were subjected to radiolabelling conditions with ^{89}Zr and the radiochemical yield of ^{89}Zr-Df-antibody was measured via iTLC and adjusted for free ^{89}Zr.

Following conjugation, each antibody conjugate was trace radiolabelled as follows: a solution containing 51 MBq (1.38 mCi) of ^{89}Zr in 0.05 M oxalic acid (Austin Health, Cyclotron, Heidelberg, Australia) was neutralized with sodium carbonate (0.1 M, 0.43 eq relative to volume of oxalic acid containing ^{89}Zr) and buffered with HEPES at pH 7.2 (0.5 M, 2.8 eq relative to volume of oxalic acid containing ^{89}Zr). Df-bintrafusp alfa or Df-controls (300 μg) were added to the neutralized ^{89}Zr mixture to give a total reaction volume of 472 μL and reactions were incubated for 1 h at 37 °C. The mixture was then quenched with EDTA (10 mM, 0.1 eq relative to volume of oxalic acid containing ^{89}Zr). The product was purified by Amicon Ultra Centrifugal filter (Ultracel 10K, Merck Millipore, Ireland) equilibrated with sodium chloride injection BP 0.9% w/v (Pfizer, Sydney, Australia). Resultant radioconjugates were assessed for radiochemical purity, antibody integrity, and immunoreactivity by cell binding analyses using antigen-expressing cell HEK293/PD-L1 as described below.

In vitro characterization of ^{89}Zr-labelled bintrafusp alfa and controls

Radiochemical purity was determined by instant thin layer chromatography (iTLC) using silica gel impregnated glass fibre iTLC strips (Gelman Sciences, Inc., Ann Arbor, MI, USA) and 20 mM sodium citrate pH 4.8 (A) or methanol:water (1:1 + 4% trifluoroacetic acid (TFA)) (B) as mobile phase.

The immunoreactive fraction of radiolabelled bintrafusp alfa and control constructs was determined by linear extrapolation to binding at infinite antigen excess using a Lindmo assay [29] as previously described [30]. Briefly, 20 ng of radiolabelled antibody was added to 0 to 5×10^6 HEK293/PD-L1 cells in 1.0 mL of culture medium. The cells were incubated for 45 min at room temperature with continuous mixing throughout to keep the cells in suspension. Cells were harvested by centrifugation and washed three times with 1 mL of culture medium to remove unbound antibody, and pellets were measured in a gamma counter (Wizard, PerkinElmer). Percentage binding of each construct (bound (%)) to HEK293/PD-L1 cells was calculated by the formula: (cpm cell pellet / cpm added radioactive antibody) × 100. Percentage binding was graphed against HEK293/PD-L1 cell concentration. Scatchard analysis was used to calculate the apparent association constant (K_a) and number of antibody molecules bound per cell [29].

Serum stability was assessed by incubating 5 μg ^{89}Zr-Df-bintrafusp alfa or controls in 100 μL of human serum at 37 °C for a 7-day period. Typical volumes for this serum mixture were approximately 105 μL, with the sample activity being dependent on the specific activity of each labelled construct. Radiochemical purity and single-point immunoreactivity

assays at 0 (day of radiolabelling, no incubation), 2, and 7 days of incubation were performed. HEK293/PD-L1 cells (2.5×10^6) were used in the single-point binding assays under conditions of antigen excess as described above in the Lindmo assay. At each time point, a sample was taken from the serum mixture and diluted in saline to formulate a 1 ng/μL solution of ^{89}Zr-Df-antibody. In total, 20 μL of this solution was added to HEK293/PD-L1 cells for the determination of immunoreactive fraction.

Radioconstruct integrity was assessed by size-exclusion chromatography high-performance liquid chromatography (SEC-HPLC). SEC-HPLC analyses were performed using an Agilent 1200 series HPLC system with a micro degasser, binary pump, and diode array detector (DAD). Scintillation traces were recorded using a Packard Canberra Flo-one Beta 150TR flow scintillation analyser. A Phenomenex BioSep 5 μm SEC-s3000 column including GFC 3000 guard column was used as the stationary phase and 50 mM PBS pH 7.2 + 5% isopropanol + 0.02% sodium azide served as the mobile phase. Chromatograms were analysed using Agilent ChemStation (Rev. B.04.03-SP2).

Animal models

In vivo investigations were performed in EMT-6 tumour-bearing mice. As a syngeneic model, EMT-6 murine cells (0.2×10^6 cells in 100-μL tissue culture medium were injected subcutaneously in the left abdominal area of 4- to 6-week-old BALB/cArc immunocompetent mice (Animal Research Centre, WA, Australia). Tumour volumes were measured by the use of a calliper. Tumour volume (TV) was calculated by the formula:

$$\mathrm{TV} = \frac{L \times W^2}{2}$$

where L is the tumour length and W is the tumour width.

Biodistribution studies

BALB/c mice with established EMT-6 tumours (TV = 384.02 ± 89.03 mm^3) received intravenous injections of ^{89}Zr-Df-bintrafusp alfa or antibody controls (^{89}Zr-Df-bintrafusp alfa (5.0 μg, 0.624 MBq (16.85 μCi); $n = 30$ mice); ^{89}Zr-Df-avelumab (5.0 μg, 0.588 MBq (15.90 μCi); $n = 10$ mice); ^{89}Zr-Df-trap control (5.0 μg, 0.551 MBq (14.90 μCi); $n = 10$ mice); or ^{89}Zr-Df-isotype control (5.0 μg, 0.710 MBq (19.2 μCi); $n = 10$ mice)). At designated time points after injection of the ^{89}Zr-Df-bintrafusp alfa radioconjugate, groups of mice ($n = 5$) were sacrificed by over-inhalation of isoflurane anaesthesia and biodistribution was assessed on day 0 (2 h), 1, 2, 3, 5, or 7 post injection. Mice injected with control antibodies were assessed at day 2 and 7 post injection only. Mice were exsanguinated by cardiac puncture, and tumours and organs (liver, spleen, kidney, muscle, skin, bone (femur), lungs, heart, stomach, brain, small intestines, large intestines, tail, and colon) were collected immediately. All samples were counted in a dual-channel gamma scintillation counter (Wizard, PerkinElmer, Australia). Triplicate standards prepared from the injected material were counted at each time point with tissue and tumour samples enabling calculations to be corrected for the physical decay of the isotope. The tissue distribution data were calculated as the mean ± SD percent injected dose per gram tissue (%ID/g) for each construct per time point.

EMT-6 competition biodistribution and PET/CT imaging study

On the day of radioconjugate synthesis, BALB/c mice with established EMT-6 tumours (TV = 158.92 ± 49.28 mm^3, n = 60) received intravenous injections of ^{89}Zr-Df-bintrafusp alfa or antibody controls. Groups of mice ($n = 10$) received a dose of ^{89}Zr-Df-bintrafusp alfa (35.0 μg, 91.0 μCi) alone or in combination with 1000 μg bintrafusp alfa, 1000 μg avelumab, or 1000 μg trap control. For each group, PET imaging and CT imaging were performed on day 2 and day 7 post injection in two animals using small animal nanoPET/MR and nanoSPECT/CT hybrid imaging systems (nanoScan®, Mediso, Budapest, Hungary). After completion of imaging at each time point, five animals per group were analysed using a biodistribution study as described before.

All PET raw data were dead-time, random, and attenuation corrected. The volumetric images were reconstructed with a transaxial matrix size of 255 × 255, using the built-in quasi Monte Carlo simulation algorithm combined with filtered sampling and stochastic iteration.

The Mediso PET camera has a specification spatial resolution of 0.9 mm; however, due to the average positron kinetic energy for ^{89}Zr (402.7 keV) [31] compared to ^{18}F (252 keV) [32], a partial volume effect characterization measurement was performed. For ^{89}Zr, this results in a positron range of 1.27 mm [32] compared to 0.66 mm for ^{18}F [31]. A series of measurements using a solution of ^{89}Zr with a concentration of 1 kBq/mL were undertaken utilizing volumes ranging from 5 to 1000 μL. The resultant recovery coefficient (RC) curve was parameterized to allow the RC value to be determined for a given lesion volume. Lesion volumes ranged from 100 to 850 μL with corresponding RCs of 45% to 100% (Online Resource Fig. 1). Based on the positron range of ^{89}Zr range determined by Jødal [31], the resultant PET spatial resolution for ^{89}Zr was calculated to be 1.5 mm. In order to account for the loss of localization of uptake due to the positron range, a deconvolution algorithm was applied to the data. The Richardson-Lucy [33, 34] algorithm was applied and the optimal parameters were found to be a 3D Gaussian with 2-mm FWHM with 5 iterations.

The co-registration of multimodality scans, generation of maximum intensity projection (MIP) PET images, and surface rendering of CT images were performed using PMOD 3.8 (PMOD Technologies LLC, Zurich, Switzerland). PET images were normalized using the standard uptake value (SUV), where SUV is a semi-quantitative index and defined as:

$$SUV(kg/mL) = \frac{C_t(kBq/mL) \times 2^{\frac{t}{\tau}}}{\frac{Injected\ Dose\ (MBq)}{Body\ Mass\ (kg)}}$$

where C_t is the radioactivity concentration (kBq/mL) in a specific image voxel at time t (h) after injection, τ is the ^{89}Zr decay half-life (78.41 h), ID is the injected dose (MBq), and BM is the body mass (kg).

Imaging analysis was performed on the series of PET/CT images acquired. Uptake (kBq/cc) in organs was determined by mark-up of volumes of interest (VOI) in cross-sectional PET/CT images. Organ volumes (mL) were determined based on mark-up of VOI in cross-sectional CT images. To convert (kBq/cc)/mL to %ID/mL, total uptake (kBq/cc) in an imaged standard was measured as an approximation of injected dose (ID). The uptake in organs of each mouse was decay corrected for to the time interval between each imaged mouse and the standard.

Immunohistochemical analysis of PD-L1 and TGF-β1 targets in EMT-6 tumour-bearing BALB/c mice

Tissues collected from EMT-6 xenograft-bearing mice at study endpoint were formalin-fixed, paraffin-embedded, and sectioned at 4-μm thickness. Antigens were retrieved by incubating sections in Target Retrieval Solution, pH 9 (Dako, Australia) in a 100 °C water bath for 20 min. Endogenous peroxidase was quenched with 3% H_2O_2 for 10 to 15 min, followed by non-specific blocking with 5% BSA in Tris-buffered saline before probing with antibodies against PD-L1 (1:100, 1 h at RT, Cell Signaling Technology, clone E1L3N) or TGF-β1 (1:200, overnight at 4 °C, Abcam, clone EPR21143). Anti-rabbit SignalStain® Boost IHC Detection reagent (Cell Signaling Technology, Australia) and anti-rabbit EnVision+ Peroxidase system (Dako, Australia) were used to detect PD-L1 and TGF-β1 primary antibodies respectively. Sections were counterstained with haematoxylin. All slides were scanned using an Aperio ScanScope slide scanner at × 20 magnification unless specified differently.

Statistical analysis

A two-sided unpaired *t*-test was used to determine significant differences between ^{89}Zr-labelled bintrafusp alfa and antibody controls. For multiple comparisons, one-way ANOVA was used with Tukey's multiple comparison test. Analyses were conducted with GraphPad Prism (Prism 8). Data are presented as mean ± SD, unless stated differently.

Results

Chelation of bintrafusp alfa and controls

Chelation of bintrafusp alfa and three controls was achieved without loss of structural integrity, as shown by SDS-PAGE analysis under reducing and non-reducing conditions (Online Resource Fig. 2). The three controls included avelumab, an anti-PD-L1 human IgG1 control antibody; isotype control; a mutated inactive anti-PD-L1 control antibody; and finally a TGF-β trap control, consisting of a mutated inactive anti-PD-L1 human IgG1 antibody fused to an active TGF-βRII. Different reaction conditions for the conjugation of Df-SCN to bintrafusp alfa or avelumab were investigated. Radiolabelling of Df-antibodies prepared at 37 °C for 1 h showed higher radiochemical yields compared to conjugates prepared at 4 °C for over 64 h. Purification of ^{89}Zr-labelled conjugates using a PD-10 desalting column or spin filtration was compared directly by splitting the crude reaction mixture into two portions. Centrifugal filtration resulted in higher specific activities and higher radiochemical purities and was chosen for further productions (Online Resource Table 2). Conjugates were purified using dialysis after it was found that purification by spin filtration leads to significantly reduced stability of the radiolabelled antibodies as shown by lower radiochemical purity and almost total loss of binding to HEK293/PD-L1 cells (Online Resource Table 3). Chelator-to-antibody ratios of Df-bintrafusp alfa, Df-avelumab, Df-trap control, and Df-isotype control were found to be 0.55 ± 0.03, 1.14 ± 0.02, 0.77 ± 0.04, and 1.14 ± 0.07, respectively (Online Resource Table 4).

Intact binding function to PD-L1 binding after chelation was assessed for Df-bintrafusp alfa and Df-avelumab by FACS analysis using HEK293/PD-L1 cells. Both Df-bintrafusp alfa and Df-avelumab retained PD-L1 binding after chelation (Fig. 1a).

Intact function of chelated constructs containing TGF-βRII as a TGF-β trap (Df-bintrafusp alfa and Df-trap control) was evaluated by ELISA (Fig. 1b). Both Df-bintrafusp alfa and Df-trap control retained binding to plate-bound TGF-β1 and TGF-β3, but not to plate-bound TGF-β2, similar to the original bintrafusp alfa [16].

Radiolabelling of Df-bintrafusp alfa and controls

All radiolabelled antibody constructs demonstrated high radiochemical purity and specific activity after labelling with ^{89}Zr (Table 1, Online Resource Fig. 3). SEC-HPLC analysis

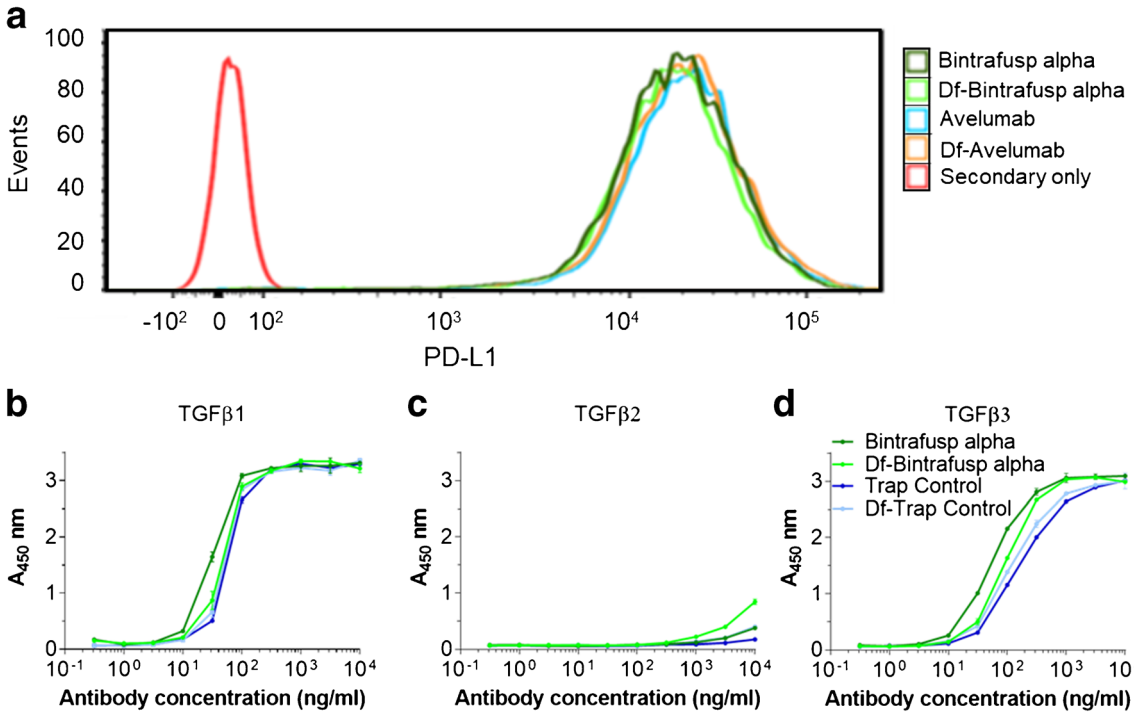

Fig. 1 Binding analysis of Df-bintrafusp alfa and Df-controls. **a** Flow cytometry analysis showing PD-L1 binding of Df-bintrafusp alfa and Df-avelumab conjugates is retained. PD-L1 binding of bintrafusp alfa, Df-bintrafusp alfa, avelumab, and Df-avelumab was determined using HEK293/PD-L1 cells. **b** ELISA assessment of TGF-β isoforms binding by bintrafusp alfa, Df-bintrafusp alfa, trap control, and Df-trap control. TGF-β1 and TGF-β3 binding specificity following Df-chelate conjugation of both Df-bintrafusp alfa and Df-trap control was maintained. Negligible binding to TGF-β2 was observed. *Bars*, mean ± SD; $n = 3$

of ^{89}Zr-Df-antibodies showed very good antibody integrity with low amounts of aggregates (Online Resource Figs. 4 and 5). HEK293/PD-L1 cells were used in single-point immunoreactivity assays to assess the PD-L1 binding of all constructs following each synthesis and before an in vivo experiment was performed (Table 1). ^{89}Zr-Df-bintrafusp alfa and ^{89}Zr-Df-avelumab showed high immunoreactivity to HEK293/PD-L1 cells and low non-specific binding was observed with non-PD-L1 binding constructs (^{89}Zr-Df-isotype control and ^{89}Zr-Df-trap control) (Table 2).

PD-L1 binding of ^{89}Zr-Df-bintrafusp alfa and ^{89}Zr-Df-avelumab was further characterized via Lindmo and Scatchard analysis (Fig. 2). ^{89}Zr-Df-bintrafusp alfa and ^{89}Zr-Df-avelumab had a similar K_a of 11.7×10^9 M^{-1} and 14.85×10^9 M^{-1} respectively. The number of binding sites per cell determined with ^{89}Zr-Df-bintrafusp alfa was 424,000 versus 411,270 with ^{89}Zr-Df-avelumab. Stability analysis of ^{89}Zr-Df-bintrafusp alfa and ^{89}Zr-Df-avelumab in human serum showed that the radiochemical purity remained high at 88.3 ± 5.7% versus 93.1 ± 5.7% respectively after 7 days of incubation in human serum (Table 2). The immunoreactivity decreased to 50.4 ± 22.5% for ^{89}Zr-Df-bintrafusp alfa versus 57.9 ± 26.0% for ^{89}Zr-Df-avelumab after 7 days of incubation in human serum (Table 2). SEC-HPLC analysis of ^{89}Zr-Df-bintrafusp alfa serum stability samples showed high stability of the construct towards aggregation. The amount of free ^{89}Zr increased from 4.9 to 13.3% over the 7-day incubation period (Online Resource Fig. 6).

Table 1 Radiochemical properties of ^{89}Zr-Df-bintrafusp alfa and controls

^{89}Zr-Df-antibody	Radiochemical purity (%)*,**	Specific activity (MBq/mg)*	Immunoreactivity (%)*
Bintrafusp alfa	97.9 ± 2.4	103.2 ± 38.9	90.8±4.5
Avelumab	98.8 ± 1.2	89.9 ± 31.5	82.4±12.0
Trap control	98.3 ± 2.7	82.9 ± 31.5	3.1±1.5
Isotype control	98.4 ± 2.5	95.5 ± 39.6	2.7±1.5

*Data presented as mean ± SD, $n = 5$ (bintrafusp alfa and avelumab) and $n = 4$ (trap and isotype control); **mobile phase A was used in iTLC

Table 2 Serum stability properties of ^{89}Zr-Df-bintrafusp alfa and ^{89}Zr-Df-avelumab over 7 days of incubation at 37 °C

In vitro test	^{89}Zr-Df-antibody	
	Bintrafusp alfa*	Avelumab*
Radiochemical purity (%)**		
D0	97.9 ± 2.4	98.8 ± 1.2
D2	93.8 ± 5.3	96.9 ± 1.9
D7	88.3 ± 5.7	93.1 ± 6.1
Immunoreactivity (%)		
D0	90.8 ± 4.5	82.4 ± 12.0
D2	68.7 ± 16.7	68.4 ± 18.9
D7	50.4 ± 22.5	57.9 ± 26.0

*Data presented as mean ± SD, $n = 5$; **mobile phase A was used in iTLC

Biodistribution studies with ^{89}Zr-Df-bintrafusp alfa and controls in EMT-6 tumour-bearing mice

In a first biodistribution study, tumour and tissue distribution of 5 μg ^{89}Zr-Df-bintrafusp alfa (0.215 MBq (5.80 μCi)) was evaluated in EMT-6 tumour-bearing BALB/c mice (Fig. 3). At this dose level, rapid blood clearance was observed with only 0.57 ± 0.13 %ID/g bintrafusp alfa remaining in the blood after 48 h suggesting the presence of an antigen sink. Highest uptake was seen in lung, spleen, liver, and kidneys. Tumour uptake was highest at 2 h post injection (6.81 ± 0.81 %ID/g) and declined over time. An increase in bone uptake over time was demonstrated and this is consistent with the release of non-chelated ^{89}Zr which has a strong affinity for phosphate and has bone-seeking properties in mice [35]. However, due to the presence of immune cells in the bone marrow, the presence of PD-L1 and TGF-β targets may contribute to the bone uptake of ^{89}Zr-Df-bintrafusp alfa observed.

To further investigate if PD-L1 binding, TGF-β binding, or both contributed to an antigen sink, tumour uptake and tissue distribution of 5 μg ^{89}Zr-Df-bintrafusp alfa (0.215 MBq (5.80 μCi)) were compared to control antibodies (5 μg ^{89}Zr-Df-avelumab, 0.204 MBq (5.50 μCi); 5 μg ^{89}Zr-Df-trap control, 0.194 MBq (5.25 μCi); 5 μg ^{89}Zr-Df-isotype control, 0.222 MBq (5.99 μCi)) on day 2 and day 7 post injection (Fig. 4, Online Resource Fig. 7, Online Resource Fig. 8). This study showed that the tumour uptake of the bifunctional bintrafusp alfa construct is driven by the PD-L1 binding sites. ^{89}Zr-Df-bintrafusp alfa and ^{89}Zr-Df-avelumab displayed a similar uptake in PD-L1-rich organs such as the lung and spleen compared to the non-PD-L1-binding isotype control. As a result, a significant increase in blood activity as well as a reduction in lung and spleen uptake was seen with the isotype control both on day 2 and day 7 post injection compared to ^{89}Zr-Df-bintrafusp alfa and ^{89}Zr-Df-avelumab. Similarly, the trap control, which also has an abrogated PD-L1 binding site but still has an active TGF-βRII site, shows a significant reduction in lung uptake and a significant increase in blood activity. Despite an increase in blood activity, the active

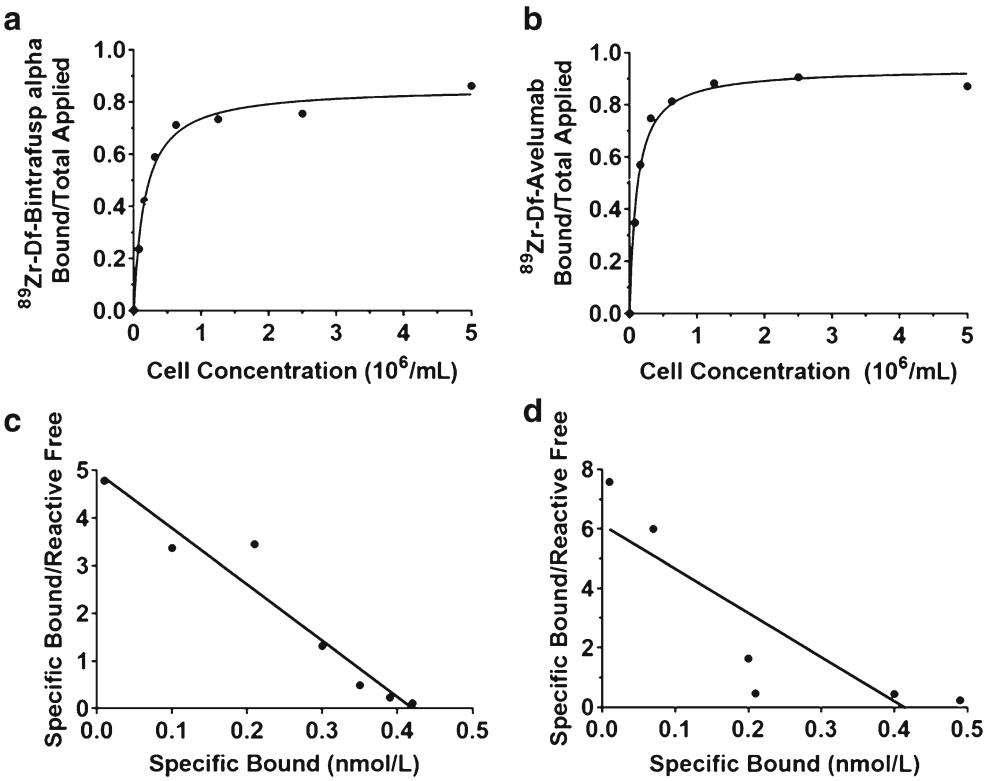

Fig. 2 In vitro characterization of PD-L1 binding of ^{89}Zr-Df-bintrafusp alfa and ^{89}Zr-Df-avelumab. **a**, **b** Lindmo plots showing binding of ^{89}Zr-Df-bintrafusp alfa (**a**) and ^{89}Zr-Df-avelumab (**b**) to increasing concentrations of PD-L1-expressing HEK293/PD-L1 cells. **c**, **d** Scatchard plots of ^{89}Zr-Df-bintrafusp alfa (**c**) and ^{89}Zr-Df-avelumab (**d**) using HEK293/PD-L1 cells. $n = 1$

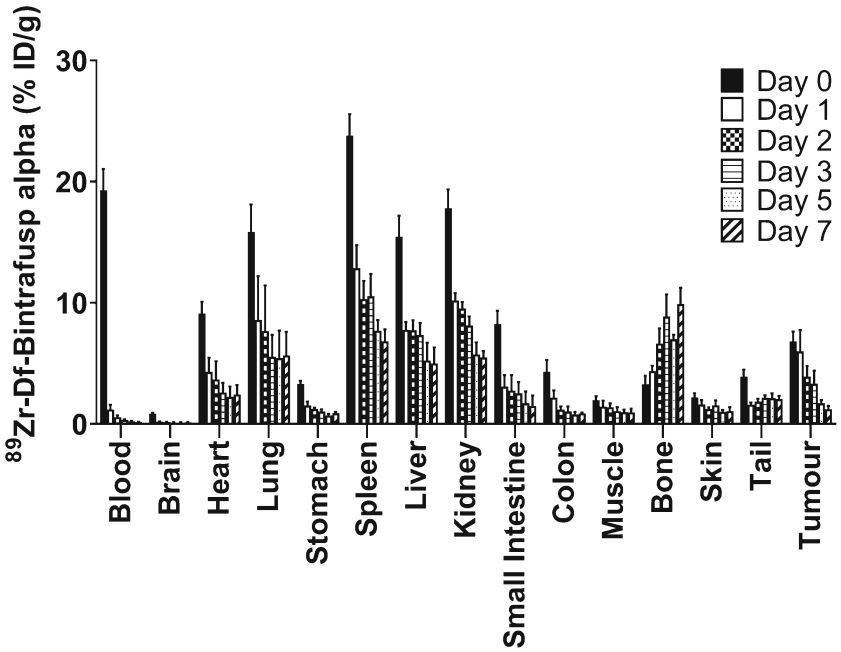

Fig. 3 Biodistribution properties of 5 μg ^{89}Zr-Df-bintrafusp alfa in EMT-6 tumour-bearing BALB/c mice over 7 days (*bars*; mean ± SD; $n = 5$)

TGF-βRII binding site of the trap control is not sufficient to increase the tumour uptake compared to the isotype control. This might be due to the significantly higher spleen, liver, kidney, and bone uptake displayed by the trap control due to the expression of TGF-β isoforms in these tissues, or partially released TGF-β. Immunohistochemical analysis of EMT-6 tumours and tissues collected from EMT-6 tumour-bearing BALB/c mice injected with ^{89}Zr-Df-bintrafusp alfa at end-point confirmed the presence of both TGF-β1 (Online Resource Fig. 9) and PD-L1 (Online Resource Fig. 10) targets in tumour, spleen, lung, liver, kidney, small intestines, duodenum, and to a lesser extent brown adipose tissue (BAT). Lastly, specific tumour uptake of ^{89}Zr-Df-bintrafusp alfa and ^{89}Zr-Df-avelumab is evident when comparing the tumour-to-blood ratios. Significantly higher tumour-to-blood ratios are seen with ^{89}Zr-Df-bintrafusp alfa and ^{89}Zr-Df-avelumab compared to ^{89}Zr-Df-trap control and ^{89}Zr-Df-isotype control on day 2 (Fig. 4b) and day 7 (Fig. 4d) post injection.

In a final biodistribution study, the influence of protein dose on tumour uptake and the specificity of ^{89}Zr-Df-bintrafusp alfa were further investigated (Fig. 5). Figure 5 shows the biodistribution results at different dose levels in the EMT-6 tumour model: 5 μg (0.25 mg/kg) ^{89}Zr-Df-bintrafusp alfa used in biodistribution studies, 35 μg (1.75 mg/kg) ^{89}Zr-Df-bintrafusp alfa used in imaging studies, 35 μg (1.75 mg/kg) ^{89}Zr-Df-bintrafusp alfa plus 1000 μg (50 mg/kg) non-radioactive trap control, 35 μg (1.75 mg/kg) ^{89}Zr-Df-bintrafusp alfa plus 1000 μg (50 mg/kg) non-radioactive bintrafusp alfa to allow competition of the radioactive imaging dose, and 35 μg (1.75 mg/kg) ^{89}Zr-Df-bintrafusp alfa plus 1000 μg (50 mg/kg) avelumab. On day 2 and day 7 post injection, blood uptake increased with higher doses. At the 35 μg dose, the highest tumour uptake (27.52 ± 5.29 %ID/g) was seen on day 2 post injection (Fig. 5, Online Resource Fig. 11). This dose also resulted in the highest tumour-to-blood ratio (58.4 ± 29.6) seen on day 7 (Online Resource Fig. 11). However, a further increase observed in spleen activity was observed, which could be due to migration of PD-L1 cells into the spleen, or incomplete target engagement. With the addition of an excessive amount of non-radioactive bintrafusp alfa (1000 μg), a significant decrease in spleen and bone uptake was observed on day 2 (Online Resource Fig. 12) and day 7 (Online Resource Fig. 13) post injection indicating effective blocking of the PD-L1 and TGF-β targets in these tissues at this dose level, resulting in high blood activity. A reduction in tumour uptake was also seen at day 2, indicative of selective binding of the labelled ^{89}Zr-Df-bintrafusp alfa blocked by excess of cold bintrafusp alfa. At day 7, the improved tumour uptake is attributed to excess antibody occupying sites in the spleen, lung, and bone, allowing more labelled antibody to reach the tumour.

Imaging studies with ^{89}Zr-Df-bintrafusp alfa in EMT-6 tumour-bearing mice

Tumour uptake of 35 μg ^{89}Zr-Df-bintrafusp alfa determined by PET image analysis was highly concordant with biodistribution results on day 7 post injection (Fig. 6). The addition of 1000 μg trap control did not change the biodistribution pattern of ^{89}Zr-Df-bintrafusp alfa significantly (Fig. 6c, d, i, j). In the absence of competing cold bintrafusp alfa (Fig. 6a, b), highest tumour uptake was seen on day 2 post injection with reduced tumour uptake seen on day 7. In the presence of 1000 μg bintrafusp alfa, the higher blood pool

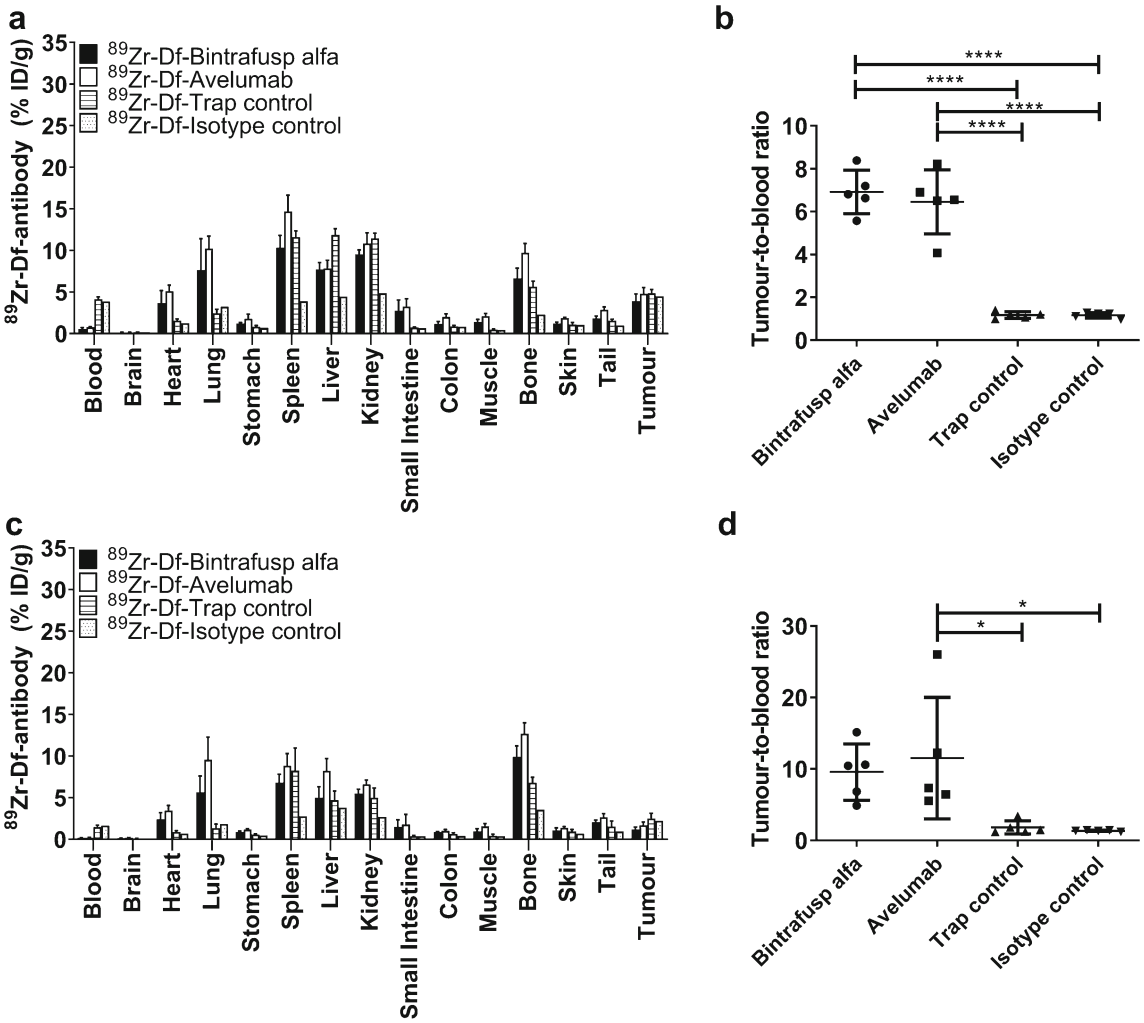

Fig. 4 Biodistribution properties of 5 μg ^{89}Zr-Df-bintrafusp alfa and controls in EMT-6 tumour-bearing BALB/c mice. **a** Tissue uptake on day 2 post injection. **b** Tumour-to-blood ratios on day 2 post injection. **c** Tissue uptake on day 7 post injection. **d** Tumour-to-blood ratios on day 7 post injection. Statistical analysis of biodistribution data is shown in Online Resources Fig. 3 and Fig. 4. *bars*; mean ± SD; $n = 5$

activity is evident from increased uptake in the heart and lungs on day 2 post injection (Fig. 6e). In addition, in the presence of competing non-radioactive bintrafusp alfa antibody, an increase in liver uptake as well as a reduction in bone activity was also confirmed by PET imaging analysis on day 7 post injection (Fig. 6f, i, j). Imaging of ^{89}Zr-Df-bintrafusp alfa in the presence of cold anti-PD-L1 antibody avelumab resulted in highly comparable changes in biodistribution pattern on day 2 and day 7 (Fig. 6g, h) supporting the finding of a previous biodistribution study (Fig. 4) that tissue distribution of bintrafusp alfa is mainly dominated by the PD-L1 binding site.

Discussion

The ability of cancer cells to evade the immune system is one of the most deadly characteristics of the majority of malignant tumours [36]. Accordingly, the recent development of antibodies which target tumour cell evasion of immune checkpoints such as the cytotoxic T lymphocyte–associated antigen-4 (CTLA-4) as well as the programmed cell death protein (PD-1) and the PD-1 ligand (PD-L1) has been a very effective approach in the treatment and/or eradication of some highly malignant forms of cancers [4, 5]. Unfortunately, not all cancers respond equally well, and the success rate and toxic side effects are unpredictable [4–10, 12]. Over the past decade, research aimed at identifying how cancer interacts with the immune system has identified several escape mechanisms that can lead to inhibition of the immune system [37]. Whilst induction of adaptive immune resistance through inhibitory receptors such as PD-1 is one mechanism cancers use, other mechanisms such as the establishment of an immunosuppressive tumour microenvironment via cytokine production (e.g. TGF-β, VEGF) can occur at the same time. With US Food and Drug Administration (FDA) approvals of anti-PD-1 and anti-PD-L1 therapeutic antibodies, the next-generation PD-L1

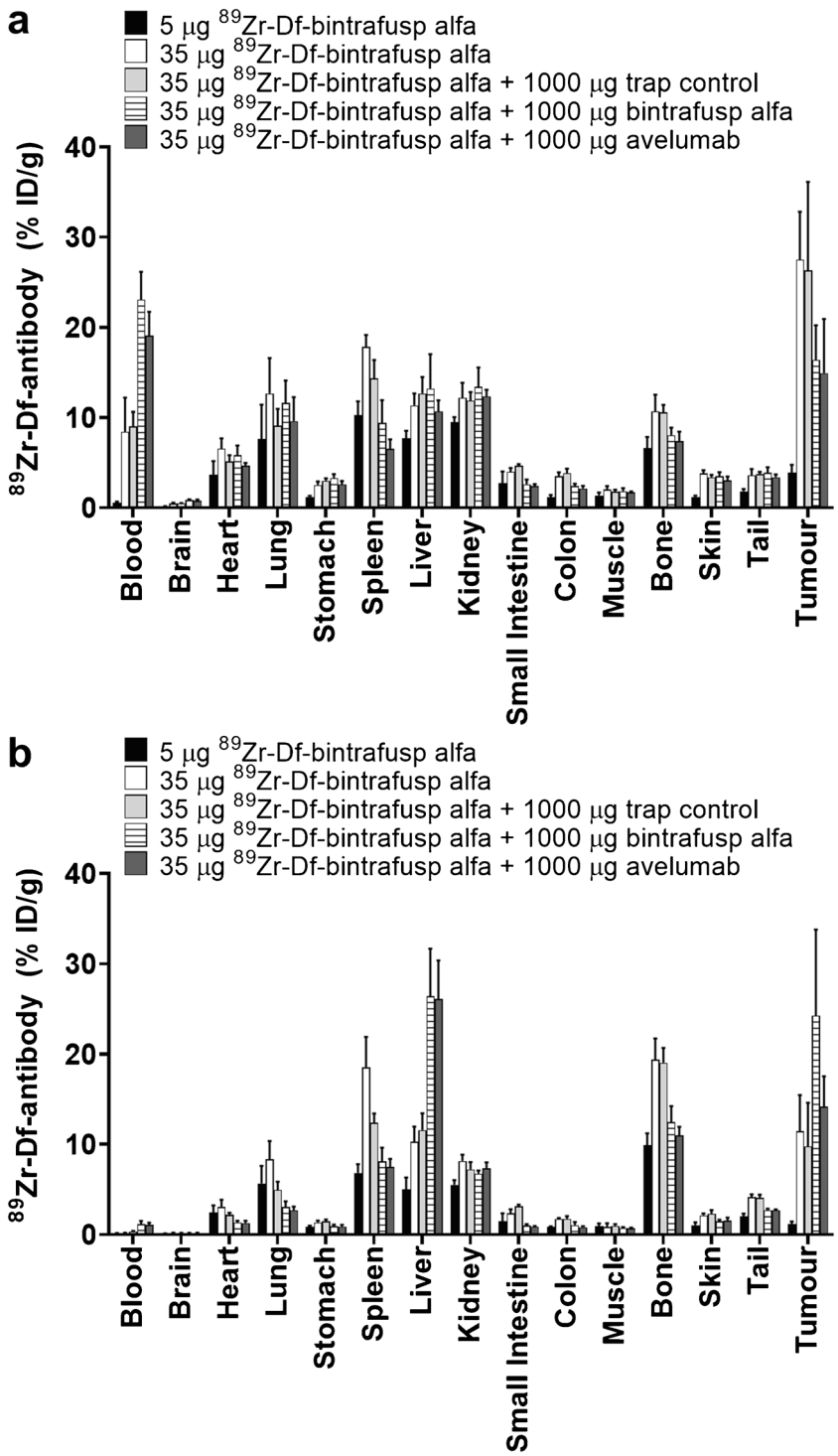

Fig. 5 Influence of protein dose on tumour uptake of ^{89}Zr-Df-bintrafusp alfa in EMT-6 tumour-bearing BALB/c mice on day 2 (**a**) and day 7 (**b**) post injection (*bars*; mean ± SD; $n = 5$). *, $P < 0.05$; **, $P < 0.01$; ***$P < 0.001$

targeting molecules currently under development encompass targeting of multiple immunosuppressive pathways simultaneously. One such molecule, bintrafusp alfa, is a bifunctional anti-PD-L1/TGF-βRII fusion protein that allows simultaneous targeting and inhibition of the complementary immunosuppressive functions of PD-L1 and TGF-β [15, 17, 18]. To aid with patient selection and quantification of dynamic changes in PD-L1 expression in upcoming clinical trial studies of bintrafusp alfa, there is a need for non-invasive detection methods of bintrafusp alfa biodistribution.

The current study has completed the preclinical radiolabelling and characterization of ^{89}Zr-Df-bintrafusp alfa. Conditions for the chelation and radiolabelling of bintrafusp alfa and avelumab, trap control, and isotype control antibody

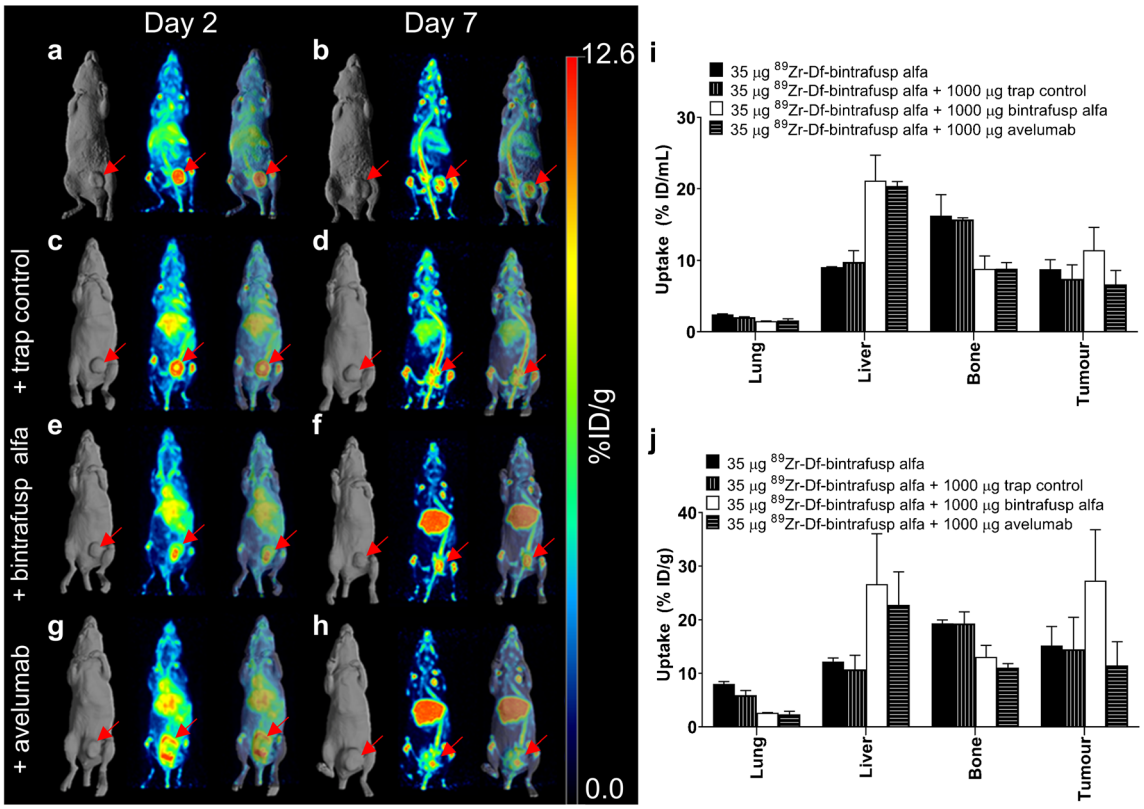

Fig. 6 From left to right, each panel shows a surface-rendered CT image, maximum intensity projection PET image, and the PET/CT overlay for representative EMT-6 tumour-bearing BALB/c mice; arrows show location of tumour. **a**, **b** 35 μg ^{89}Zr-Df-bintrafusp alfa on day 2 (**a**) and day 7 (**b**). **c**, **d** 35 μg ^{89}Zr-Df-bintrafusp alfa with excess 1000 μg cold M7284 on day 2 (**c**) and day 7 (**d**). **e**, **f** 35 μg ^{89}Zr-Df-bintrafusp alfa with excess 1000 μg cold avelumab on day 2 (**e**) and day 7 (**f**). **g**, **h** 35 μg ^{89}Zr-Df-bintrafusp alfa with excess trap control on day 2 (**g**) and day 7 (**h**). **i** Quantitation of ^{89}Zr-Df-bintrafusp alfa uptake in the lung, liver, bone, and tumour tissues via PET analysis of imaged mice on day 7 post injection (*bars*; mean ± SD; $n = 2$). **j** Quantitation of ^{89}Zr-Df-bintrafusp alfa uptake in the lung, liver, bone, and tumour tissues via biodistribution analysis of imaged mice on day 7 post injection (*bars*; mean ± SD; $n = 2$)

constructs were determined to produce active and stable radioconjugates. No differences were observed in the in vitro binding properties of ^{89}Zr-Df-bintrafusp alfa and ^{89}Zr-Df-avelumab and radiolabelling did not interfere with the PD-L1-positive cell binding properties of the radioconjugates. The chelation chemistry did not impact the protein integrity and PD-L1 or TGF-β binding properties of bintrafusp alfa.

The nanomolar affinities seen with ^{89}Zr-Df-bintrafusp alfa and ^{89}Zr-Df-avelumab are in good agreement with prior affinity measurements with the HEK293/PD-L1 cell line by FACS for bintrafusp alfa (EC_{50} of 48 ng/mL (0.27 nM,)) and avelumab (EC_{50} 34 ng/mL (0.24 nM)) [16]. ELISA results with mock radiolabelled bintrafusp alfa and trap control were in alignment with previous findings with plate-bound human TGF-β1 and TGF-β3 ($EC_{50} = 215.3$ and 651.4 ng/mL, respectively), but not plate-bound TGF-β2, due to low intrinsic binding affinity between TGF-β2 and TGF-βRII [16]. Furthermore, ^{89}Zr-Df-bintrafusp alfa was prepared with high radiochemical purity (97.9 ± 2.4%), specific activity (103.2 ± 38.9 MBq/mg), and PD-L1 cell binding immunoreactivity (90.8 ± 4.5%). These properties were highly comparable to the radiochemical properties of ^{89}Zr-Df-avelumab control. All four radioconjugates demonstrated good stability when incubated in human serum for 7 days at 37 °C with retention of the radioconjugate's immunoreactivities, integrity, and radiochemical purities.

To compare the biodistribution of ^{89}Zr-Df-bintrafusp alfa to an approved anti-PD-L1 antibody, we utilized radiolabelled avelumab as a positive control within the study. The radiolabelled forms of inactive PD-L1 antibody mutant fused to TGF-βRII and an inactive PD-L1 antibody isotype negative control were also optimized and included in the study. The pattern of biodistribution observed for ^{89}Zr-Df-bintrafusp alfa and ^{89}Zr-Df-avelumab was highly comparable to published biodistribution and imaging studies of other PD-L1 targeting antibodies [21–24, 26, 38] indicating that the tissue distribution pattern of ^{89}Zr-Df-bintrafusp alfa is dominated by its PD-L1 binding site, and the construct size of bintrafusp alfa does not impede tumour uptake. The presence of excessive unlabelled antibody decreased splenic and lung uptake effectively, improving the uptake of bintrafusp alfa in the tumour. This provides an opportunity to use this reagent both in diagnostic and therapeutic applications in a theranostic approach.

Different protein concentrations of bintrafusp alfa were evaluated in this study, and the impact of increasing protein doses on biodistribution will be further assessed in the human bioimaging trial.

Because bintrafusp alfa followed the biodistribution pattern of a PD-L1 targeting antibody, our studies confirmed previous findings in immunocompetent mice that the spleen and lung are a significant sink for PD-L1 targeting antibody constructs with the amount available in the tumour environment impacted by splenic and lung uptake [38, 39]. The presence of PD-L1 in the lung and spleen was confirmed via immunohistochemical analysis. PD-L1 showed heterogeneous expression patterns in the EMT-6 tumours which aligns with the slightly heterogeneous tumour uptake seen in the PET/CT images and previous reports of heterogeneous PD-L1 expression in human tumours [40]. Staining of PD-L1 in mouse kidney, liver, and spleen confirmed previous findings by Josefsson et al. [24]. In agreement with these studies, dosing with 1000 μg (50 mg/kg) cold bintrafusp alfa or avelumab caused higher exposure of the tumour to circulating ^{89}Zr-Df-bintrafusp alfa leading to greater than 2-fold increased tumour uptake and reduced localization to PD-L1-rich organs of spleen and lung. Another organ that might have contributed to the sink but was not included in our study is the thymus [38].

We found that co-administration of excess bintrafusp alfa or avelumab increased ^{89}Zr-Df-bintrafusp alfa localization to the liver in normal BALB/c mice bearing EMT-6 tumours, with liver a known PD-L1-positive [41] and TGF-β-rich organ [42]. In addition, when comparing the biodistribution of ^{89}Zr-Df-trap control and the non-active PD-L1 isotype control, both antibodies showed increased blood activity compared to ^{89}Zr-Df-bintrafusp alfa or ^{89}Zr-Df-avelumab; however, the trap control showed specific higher uptake in TGF-β-rich organs such as the spleen, liver, kidney, and bone compared to the isotype control. This is in agreement with studies of human kidney specimens showing that the three major isoforms—TGF-β1, TGF-β2, and TGF-β3—are expressed in the kidneys [43]. TGF-β is also expressed in the bone marrow. Although active TGF-β is only a small percentage of the total pool of latent TGF-β (LAP/TGF-β), a recent study has shown that TGF-β may be active but still tethered to LAP [44]. Together, our data suggests that PD-L1 and potentially the TGF-β trap component are therefore involved in the biodistribution pattern of bintrafusp alfa, and the PD-L1 binding portion of bintrafusp alfa is primarily responsible for the uptake in tumour which then results in simultaneous inhibition of PD-L1 and TGF-β.

In conclusion, the Df-conjugation and ^{89}Zr-radiolabelling of bifunctional bintrafusp alfa have been optimized to produce a stable, pure, and highly immunoreactive radioconstruct that binds PD-L1, whilst maintaining the TGF-β trap function. The specificity of ^{89}Zr-Df-bintrafusp alfa localization to tumour in vivo and the impact of normal tissue PD-L1 antigen sink was demonstrated by co-administration of excess unlabelled bintrafusp alfa both via biodistribution studies and quantitative PET studies. Furthermore, PET imaging demonstrated that molecular imaging of ^{89}Zr-Df-bintrafusp alfa biodistribution was achievable, and allows non-invasive quantitation of tumour uptake of ^{89}Zr-Df-bintrafusp alfa. These results also demonstrate that ^{89}Zr-Df-bintrafusp alfa is suitable for use in bioimaging clinical trials in cancer patients, which have commenced (NCT04297748).

Supplementary Information The online version contains supplementary material available at https://doi.org/10.1007/s00259-021-05251-0.

Acknowledgements This work was supported by funding from EMD Serono Research & Development Institute, Inc., a business of Merck KGaA, Darmstadt, Germany. We acknowledge the Australian Cancer Research Foundation for providing funds to purchase the nanoPET/MRI and nanoSPECT/CT imaging equipment. This research was also undertaken using the Solid Target Laboratory, an ANSTO-Austin-LICR-ONJCRI Partnership. The support of the Operational Infrastructure Support Program of the Victorian State Government, and to AMS (NHRMC Investigator Grant 1177837) is acknowledged.

Code availability Not applicable

Author contribution All authors contributed to the study conception and design. Material preparation, data collection, and analysis were performed by Ingrid J.G. Burvenich, Yit W. Goh, Nancy Guo, Angela Rigopoulos, Diana Cao, Zhanqi Liu, Uwe Ackermann, Christian W. Wichmann, Alexander F. McDonald, Nhi Huynh, Graeme J. O'Keefe, Sylvia J. Gong, Fiona E. Scott, and Andrew M. Scott. The first draft of the manuscript was written by Ingrid J.G. Burvenich and all authors commented on all versions of the manuscript. All authors read and approved the final manuscript.

Funding This study was funded by EMD Serono/Merck KGaA.

Data availability The datasets generated during and/or analysed during the current study are available from the corresponding author on reasonable request.

Declarations

Ethics approval All animal studies were approved by the Austin Health Animal Ethics Committee and were conducted in compliance with the Australian Code for the care and use of animals for scientific purposes (8th Edition, 2013).

Consent to participate Not applicable

Consent for publication Written approval was obtained from all authors prior to submission of the paper.

Conflict of interest Linghui Li, Wanping Geng, Yan Lan, and Anup Zutshi are employees of EMD Serono Research & Development Institute, Inc., a business of Merck KGaA, Darmstadt, Germany. This work was supported by funding from EMD Serono Research & Development Institute, Inc. and Merck KGaA, Darmstadt, Germany.

References

1. Zang X, Loke P, Kim J, Murphy K, Waitz R, Allison JP. B7x: a widely expressed B7 family member that inhibits T cell activation. Proc Natl Acad Sci U S A. 2003;100:10388–92.
2. Ogawa S, Abe R. Signal transduction via co-stimulatory and co-inhibitory receptors. Adv Exp Med Biol. 2019;1189:85–133.
3. Chae YK, Arya A, Iams W, Cruz MR, Chandra S, Choi J, et al. Current landscape and future of dual anti-CTLA4 and PD-1/PD-L1 blockade immunotherapy in cancer; lessons learned from clinical trials with melanoma and non-small cell lung cancer (NSCLC). J Immunother Cancer. 2018;6:39.
4. Yang Y. Cancer immunotherapy: harnessing the immune system to battle cancer. J Clin Invest. 2015;125:3335–7.
5. Chen L, Han X. Anti-PD-1/PD-L1 therapy of human cancer: past, present, and future. J Clin Invest. 2015;125:3384–91.
6. Antonia S, Goldberg SB, Balmanoukian A, Chaft JE, Sanborn RE, Gupta A, et al. Safety and antitumour activity of durvalumab plus tremelimumab in non-small cell lung cancer: a multicentre, phase 1b study. Lancet Oncol. 2016;17:299–308.
7. Apolo AB, Infante JR, Balmanoukian A, Patel MR, Wang D, Kelly K, et al. Avelumab, an anti-programmed death-ligand 1 antibody, in patients with refractory metastatic urothelial carcinoma: results from a multicenter, phase Ib study. J Clin Oncol. 2017;35:2117–24.
8. Balar AV, Galsky MD, Rosenberg JE, Powles T, Petrylak DP, Bellmunt J, et al. Atezolizumab as first-line treatment in cisplatin-ineligible patients with locally advanced and metastatic urothelial carcinoma: a single-arm, multicentre, phase 2 trial. Lancet. 2017;389:67–76.
9. Disis ML, Taylor MH, Kelly K, Beck JT, Gordon M, Moore KM, et al. Efficacy and safety of avelumab for patients with recurrent or refractory ovarian cancer: phase 1b results from the JAVELIN Solid Tumor trial. JAMA Oncol. 2019;5:393–401.
10. Fehrenbacher L, Spira A, Ballinger M, Kowanetz M, Vansteenkiste J, Mazieres J, et al. Atezolizumab versus docetaxel for patients with previously treated non-small-cell lung cancer (POPLAR): a multicentre, open-label, phase 2 randomised controlled trial. Lancet. 2016;387:1837–46.
11. Rosenberg JE, Hoffman-Censits J, Powles T, van der Heijden MS, Balar AV, Necchi A, et al. Atezolizumab in patients with locally advanced and metastatic urothelial carcinoma who have progressed following treatment with platinum-based chemotherapy: a single-arm, multicentre, phase 2 trial. Lancet. 2016;387:1909–20.
12. Vaishampayan U, Schoffski P, Ravaud A, Borel C, Peguero J, Chaves J, et al. Avelumab monotherapy as first-line or second-line treatment in patients with metastatic renal cell carcinoma: phase Ib results from the JAVELIN Solid Tumor trial. J Immunother Cancer. 2019;7:275.
13. Walker JW, Lebbe C, Grignani G, Nathan P, Dirix L, Fenig E, et al. Efficacy and safety of avelumab treatment in patients with metastatic Merkel cell carcinoma: experience from a global expanded access program. J Immunother Cancer. 2020;8:e000313.
14. Knudson KM, Hicks KC, Luo X, Chen JQ, Schlom J, Gameiro SR. M7824, a novel bifunctional anti-PD-L1/TGFbeta trap fusion protein, promotes anti-tumor efficacy as monotherapy and in combination with vaccine. Oncoimmunology. 2018;7:e1426519.
15. Jochems C, Tritsch SR, Pellom ST, Su Z, Soon-Shiong P, Wong HC, et al. Analyses of functions of an anti-PD-L1/TGFbetaR2 bispecific fusion protein (M7824). Oncotarget. 2017;8:75217–31.
16. Lan Y, Zhang D, Xu C, Hance KW, Marelli B, Qi J, et al. Enhanced preclinical antitumor activity of M7824, a bifunctional fusion protein simultaneously targeting PD-L1 and TGF-beta. Sci Transl Med. 2018;10:eaan5488.
17. Mariathasan S, Turley SJ, Nickles D, Castiglioni A, Yuen K, Wang Y, et al. TGFbeta attenuates tumour response to PD-L1 blockade by contributing to exclusion of T cells. Nature. 2018;554:544–8.
18. Tauriello DVF, Palomo-Ponce S, Stork D, Berenguer-Llergo A, Badia-Ramentol J, Iglesias M, et al. TGFbeta drives immune evasion in genetically reconstituted colon cancer metastasis. Nature. 2018;554:538–43.
19. Lind H, Gameiro SR, Jochems C, Donahue RN, Strauss J, Gulley JM, et al. Dual targeting of TGF-beta and PD-L1 via a bifunctional anti-PD-L1/TGF-betaRII agent: status of preclinical and clinical advances. J Immunother Cancer. 2020;8:e000433.
20. Strauss J, Heery CR, Schlom J, Madan RA, Cao L, Kang Z, et al. Phase I trial of M7824 (MSB0011359C), a bifunctional fusion protein targeting PD-L1 and TGFbeta, in advanced solid tumors. Clin Cancer Res. 2018;24:1287–95.
21. Chatterjee S, Lesniak WG, Gabrielson M, Lisok A, Wharram B, Sysa-Shah P, et al. A humanized antibody for imaging immune checkpoint ligand PD-L1 expression in tumors. Oncotarget. 2016;7:10215–27.
22. Heskamp S, Hobo W, Molkenboer-Kuenen JD, Olive D, Oyen WJ, Dolstra H, et al. Noninvasive imaging of tumor PD-L1 expression using radiolabeled anti-PD-L1 antibodies. Cancer Res. 2015;75:2928–36.
23. Hettich M, Braun F, Bartholoma MD, Schirmbeck R, Niedermann G. High-resolution PET imaging with therapeutic antibody-based PD-1/PD-L1 checkpoint tracers. Theranostics. 2016;6:1629–40.
24. Josefsson A, Nedrow JR, Park S, Banerjee SR, Rittenbach A, Jammes F, et al. Imaging, biodistribution, and dosimetry of radionuclide-labeled PD-L1 antibody in an Immunocompetent mouse model of breast cancer. Cancer Res. 2016;76:472–9.
25. Lesniak WG, Chatterjee S, Gabrielson M, Lisok A, Wharram B, Pomper MG, et al. PD-L1 detection in tumors using [(64)Cu]atezolizumab with PET. Bioconjug Chem. 2016;27:2103–10.
26. Christensen C, Kristensen LK, Alfsen MZ, Nielsen CH, Kjaer A. Quantitative PET imaging of PD-L1 expression in xenograft and syngeneic tumour models using a site-specifically labelled PD-L1 antibody. Eur J Nucl Med Mol Imaging. 2020;47:1302–13.
27. Vosjan MJ, Perk LR, Visser GW, Budde M, Jurek P, Kiefer GE, et al. Conjugation and radiolabeling of monoclonal antibodies with zirconium-89 for PET imaging using the bifunctional chelate p-isothiocyanatobenzyl-desferrioxamine. Nat Protoc. 2010;5:739–43.
28. Chomet M, Schreurs M, Bolijn MJ, Verlaan M, Beaino W, Brown K, et al. Head-to-head comparison of DFO* and DFO chelators: selection of the best candidate for clinical 89Zr-immuno-PET. Eur J Nucl Med Mol Imaging. 2020. https://doi.org/10.1007/s00259-020-05002-7.
29. Lindmo T, Boven E, Cuttitta F, Fedorko J, Bunn PA Jr. Determination of the immunoreactive fraction of radiolabeled monoclonal antibodies by linear extrapolation to binding at infinite antigen excess. J Immunol Methods. 1984;72:77–89.
30. Lee FT, Rigopoulos A, Hall C, Clarke K, Cody SH, Smyth FE, et al. Specific localization, gamma camera imaging, and intracellular trafficking of radiolabelled chimeric anti-G(D3) ganglioside monoclonal antibody KM871 in SK-MEL-28 melanoma xenografts. Cancer Res. 2001;61:4474–82.
31. Jodal L, Le Loirec C, Champion C. Positron range in PET imaging: an alternative approach for assessing and correcting the blurring. Phys Med Biol. 2012;57:3931–43.
32. Jodal L, Le Loirec C, Champion C. Positron range in PET imaging: non-conventional isotopes. Phys Med Biol. 2014;59:7419–34.
33. Richardson WH. Bayesian-based iterative method of image restoration. J Opt Soc Am. 1972;62:55–9.
34. Lucy LB. An iterative technique for the rectification of observed distributions. Astron J. 1974;79:745–54.

35. Abou DS, Ku T, Smith-Jones PM. In vivo biodistribution and accumulation of 89Zr in mice. Nucl Med Biol. 2011;38:675–81.
36. Drake CG, Jaffee E, Pardoll DM. Mechanisms of immune evasion by tumors. Adv Immunol. 2006;90:51–81.
37. Teng MW, Galon J, Fridman WH, Smyth MJ. From mice to humans: developments in cancer immunoediting. J Clin Invest. 2015;125:3338–46.
38. Nedrow JR, Josefsson A, Park S, Ranka S, Roy S, Sgouros G. Imaging of programmed cell death ligand 1: impact of protein concentration on distribution of anti-PD-L1 SPECT agents in an immunocompetent murine model of melanoma. J Nucl Med. 2017;58:1560–6.
39. Deng R, Bumbaca D, Pastuskovas CV, Boswell CA, West D, Cowan KJ, et al. Preclinical pharmacokinetics, pharmacodynamics, tissue distribution, and tumor penetration of anti-PD-L1 monoclonal antibody, an immune checkpoint inhibitor. MAbs. 2016;8:593–603.
40. Parra ER, Villalobos P, Mino B, Rodriguez-Canales J. Comparison of different antibody clones for immunohistochemistry detection of programmed cell death ligand 1 (PD-L1) on non–small cell lung carcinoma. Appl Immunohistochem Mol Morphol. 2018;26:83–93.
41. Patel SP, Kurzrock R. PD-L1 expression as a predictive biomarker in cancer immunotherapy. Mol Cancer Ther. 2015;14:847–56.
42. Schon HT, Weiskirchen R. Immunomodulatory effects of transforming growth factor-beta in the liver. Hepatobiliary Surg Nutr. 2014;3:386–406.
43. Ito Y, Goldschmeding R, Kasuga H, Claessen N, Nakayama M, Yuzawa Y, et al. Expression patterns of connective tissue growth factor and of TGF-beta isoforms during glomerular injury recapitulate glomerulogenesis. Am J Physiol Ren Physiol. 2010;299:F545–58.
44. Campbell MG, Cormier A, Ito S, Seed RI, Bondesson AJ, Lou J, et al. Cryo-EM reveals integrin-mediated TGF-β activation without release from latent TGF-β. Cell. 2020;180:490–501.